Dalton Transactions

PAPER

View Article Online
View Journal | View Issue

Cite this: *Dalton Trans.*, 2026, **55**, 5139

Amplified electron–spin thermal sensitivity in Mn(II) complexes

Anthony J. Campanella, [a] Amanda Gin, [a] Siyoung Sung,[a] Cassidy E. Jackson,[a] Roxanna Martinez, [b] Ökten Üngör, [b] Srikanth Dasari, [b] Andrew Ozarowski, [c] Indrani Bhowmick [a,d] and Joseph M. Zadrozny *[b]

Received 5th December 2025,
Accepted 6th January 2026

DOI: 10.1039/d5dt02920a

rsc.li/dalton

Understanding the temperature sensitivity of magnetic resonance properties is an essential step toward any spin application, whether for novel molecular thermometers or quantum sensing platforms. Hence, demonstrations that molecular tuning is effective at modifying the temperature dependence of the electron paramagnetic resonance spectra of open-shell molecules are vital. Herein we show that ligand choice offers one handle for controlling the temperature dependence of the EPR spectrum, ostensibly through modifying the temperature sensitivity of the zero-field splitting parameter, D. For this demonstration, we prepared and analyzed three different encapsulated Mn(II) complexes. High-field, high-frequency EPR spectroscopy reveals EPR spectra for all complexes that vary in width as a function of temperature. At lower temperatures, these temperature sensitivities change starkly with the ligand shell, yielding thermal sensitivities of 2.2 to 9.8 MHz K^{-1} for D. These results suggest the ability to modify the variable temperature nature of D by ligand selection, the first time for the Mn(II) metal ion, which shows significant enhancement over the nitrogen vacancy center of a diamond lattice (*ca.* 74 kHz K^{-1}).

Introduction

The ability to design temperature-dependent electron paramagnetic resonance (EPR) signals in molecules is an important prerequisite to new temperature-sensitive quantum sensing platforms.[1,2] This is especially true in open-shell molecules, which are tunable and can be dissolved in solution, paving a path for potential spin-based EPR imaging technologies that embrace quantum controls. Long-term applications could include, *e.g.* noninvasive biomedical thermometry *via* EPR[3,4] or optically detected magnetic resonance, the latter of which currently harnesses nitrogen-vacancy (NV) center qubits.[5,6]

The knowledge to tune the temperature sensitivity of EPR parameters (*e.g.* the g factor or hyperfine coupling, A) in metal complexes is largely lacking, which precludes many of the mentioned applications. The most intuitive variable-temperature effects that one would think to exploit are the well-known spin crossover[7] and valence tautomerization (VT) phenomena.[8] Yet, these behaviors are most prevalent for ions that are EPR silent, like high- and low-spin Fe(II), or are strongly magnetically anisotropic, like Co(II). These magnetic properties are all disadvantageous for eventual application. An EPR silent system would either yield no measurable signal (*e.g.* $S = 0$) or require high-frequency microwaves to observe, the latter absorbed by aqueous tissue.[9] Strong magnetic anisotropy, in contrast, hastens spin relaxation at higher temperatures,[10] which broadens signals at room temperature and in solution to preclude detection. Hence, new ways of producing temperature-dependent EPR signals are needed, especially ones where the signal is guaranteed to be observable.

We propose one such way through the temperature dependence of zero-field splitting parameter (D) in an open-shell complex where D is already small (*e.g.* <1 cm^{-1}). Such a system is advantageous in two ways. First, the small magnitude of D precludes EPR silence and enables readout. Second, the sign and magnitude of D could vary with temperature, enabling thermal sensitivity. Indeed, the S and D of a complex dictate the number and distribution of signals in the EPR spectrum, and this parameter hinges on the symmetry and strength of the ligand field.[11] Hence, small temperature-dependent changes in M–L bond distances or angles should imbue a temperature dependence on the EPR spectra.[12–14] Analogous phenomena guide the temperature dependence of the NMR properties of metal nuclei (*e.g.* ^{59}Co) in metal complexes.[15]

To the best of our knowledge, no design strategies for temperature-dependent zero-field splitting and EPR exist, nor have

[a]*Department of Chemistry, Colorado State University, Fort Collins, CO 80523, USA*
[b]*Department of Chemistry and Biochemistry, The Ohio State University, Columbus, OH 43210, USA. E-mail: zadrozny.13@osu.edu*
[c]*National High Magnetic Field Laboratory, Tallahassee, FL 32310, USA*
[d]*Analytical Resources Core Facility, Colorado State University, Fort Collins, CO 80523, USA*

there been the necessary first-step demonstrations that molecular modification can affect that temperature dependence. Indeed, the assumption that zero-field splitting is temperature *independent* is so widely held that it defines standard methods of extracting D (and related parameters) from variable-temperature magnetic susceptibility and magnetization data.[16,17] We note that the effect of slight bond distance changes is already observed to cause the high temperature sensitivity of the D parameter (−74.2(7) kHz K^{-1}) in the NV center system.[18,19] Molecules may hold the key to even higher temperature sensitivity owing to higher structural flexibility *versus* a rigid diamond lattice, but this hypothesis needs to be tested.

Herein, we present the synthesis and investigation of a series of three Mn(II) complexes to study, for the first time, how molecular identity can affect the temperature sensitivity of a zero field splitting of the molecule. The three complexes contain Mn(II) encapsulated with cryptand-derivative ligands:[20–22] $[MnL1](PF_6)_2$ (**1**, L1 = 1,4,7,10,13,16,21,24-octaazabicyclo[8.8.8]hexacosa-4,6,13,15,21,23-hexaene), $[MnL2](PF_6)_2$ (**2**, L2 = 1,4,7,10,13,16,21,24-octaazabicyclo[8.8.8]hexacosane), and $[MnL3](PF_6)_2$ (**3**, L3 = 17,20,25,28-tetraoxa-1,14,31,32-tetraazatetracyclo[12.8.8.$1^{3,7}$.$1^{8,12}$]dotriaconta-3,5,7(32),8,10,12(31)-hexaene) (Fig. 1).

We anticipated that Mn(II) would exhibit relatively high changes in D with changes in T owing to the high-spin states and population of e_g* MOs, such that the excited-state energies contributing to the magnitude of D should be significantly affected by slight T-dependent changes in bond distances and angles. We furthermore hypothesized that Mn(II) would enable clear spectral resolution of these changes on account of its well-documented small zero-field splittings and ease of analysis by EPR. The focus on encaging ligands is motivated by the afforded kinetic stability, which, in the long term, could be leveraged for novel bioimaging applications that avoid toxicity from metal-ion release.

We find that there is a strong temperature dependence of the EPR spectra for **1**–**3** that can be modeled with a variable-temperature zero-field splitting. Excitingly, the observed temperature dependences of D are all large for **1**–**3** and eclipse the magnetic resonance thermometry sensitivities of the prototypical NV center.[18,19] The variation in this temperature-dependent behavior across the complexes is likely dictated by ligand-counterion interactions, as nearly negligible changes are observed in solution, where complex-counterion interactions are expected to be suppressed. The results thus represent an important step in understanding what molecular features control the temperature sensitivity of spin Hamiltonian parameters and therefore magnetic resonance spectra.

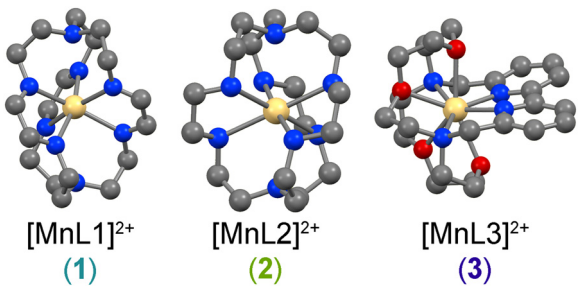

Fig. 1 Molecular structures of $[MnL1]^{2+}$, $[MnL2]^{2+}$, and $[MnL3]^{2+}$ as determined for **1**, **2**, and **3**. Yellow, red, blue, and gray spheres represent Mn, O, N, and C atoms, respectively. Hydrogens and PF_6^- counterions have been omitted for clarity.

Experimental

General considerations

L1, L2, and [(L3)Na]Br were synthesized following published procedures.[20–22] Methanol (MeOH), ethanol (EtOH), diethyl ether (Et_2O), acetonitrile (MeCN), NH_4PF_6, sucrose, and $MnCl_2{\cdot}4H_2O$ were all purchased commercially and used as received. Unless otherwise stated, compounds were handled under an ambient atmosphere.

Synthesis of $[MnL1](PF_6)_2{\cdot}H_2O$ (1)

A solution of L1 (0.309 g, 0.861 mmol) in 5 mL EtOH was added dropwise to a solution of $MnCl_2{\cdot}4H_2O$ (0.171 g, 0.866 mmol) in 5 mL EtOH and allowed to stir overnight, producing an intense orange solution and a small amount of precipitate. The mixture was evaporated to dryness, redissolved in a minimum amount (8 mL) of MeOH and filtered. The filtrate was placed in an Et_2O chamber and crystallized by vapor diffusion. The orange solid was collected and dissolved in a minimum amount (5 mL) of EtOH. This orange solution was then added to a 5 mL EtOH solution saturated with NH_4PF_6. An orange powder immediately precipitated, which was collected by vacuum filtration, washed with Et_2O, and dried under reduced pressure at 70 °C to yield **1** (0.238 g, 0.330 mmol, 38% yield). Single crystals suitable for single-crystal X-ray diffraction were grown by vapor diffusion of Et_2O into a concentrated MeCN solution of **1**. Combustion analysis, calculated for $C_{18}H_{30}N_8MnF_{12}P_2{\cdot}H_2O$: 29.97%C, 4.47%H, 15.53%N; found: 29.99%C, 4.24%H, 15.36%N. IR (cm^{-1}, diamond ATR): 2929, 2869, 2846, 1672, 1621, 1463, 1449, 1391, 1377, 1280, 1269, 1166, 1105, 1085, 1067, 1052, 999, 922, 825, 745, 622, 556, 544, 448, 423, 409. LC-MS (m/z), positive ion mode: $\{[Mn(L1)]PF_6\}^+$, 558.16. See Fig. S3 for UV-Vis characterization and Fig. S18 for comparison of powder diffraction data with simulations from single-crystal analysis.

Synthesis of $[MnL2](PF_6)_2$ (2)

A colorless MeOH solution (5 mL) of $MnCl_2{\cdot}4H_2O$ (0.138 g, 0.697 mmol) was added dropwise to a colorless EtOH solution (5 mL) of L2 (0.259 g, 0.698 mmol). The pale orange reaction mixture was stirred at room temperature under an ambient atmosphere overnight. The resulting solution was filtered through diatomaceous earth, and the filtrate was concentrated on a rotary evaporator, yielding a pale orange powder. This powder was dissolved in a minimum amount (10 mL) of EtOH and crystallized from this solution *via* slow evaporation. The pale orange solid was then dissolved in a minimum amount

(5 mL) of EtOH and added to 5 mL EtOH solution saturated with NH_4PF_6. A very pale orange powder immediately precipitated, which was collected by vacuum filtration, washed with Et_2O, and dried under reduced pressure to yield **2** (0.213 g, 0.297 mmol, 42% yield). Single crystals suitable for single-crystal X-ray diffraction were grown by diffusion of Et_2O vapor into a concentrated MeCN solution of **2**. Combustion analysis, calculated for $C_{18}H_{36}N_8MnF_{12}P_2$: 30.22%C, 5.92%H, 15.66%N; found: 30.47%C, 5.94%H, 15.68%N. IR (cm^{-1}, diamond ATR): 3336, 2980, 2928, 2877, 2841, 1472, 1452, 1376, 1360, 1304, 1269, 1158, 1100, 1067, 959, 936, 881, 833, 815, 798, 597, 556, 510, 426. LC-MS (*m*/*z*), positive ion mode: $\{[Mn(L2)]PF_6\}^+$, 570.25. See Fig. S3 for UV-Vis characterization and Fig. S18 for comparison of powder diffraction data with simulations from single-crystal analysis.

Synthesis of $[MnL3](PF_6)_2 \cdot 0.5MeCN$ (3)

A solution of $MnCl_2 \cdot 4H_2O$ (0.250 g, 1.264 mmol) in 30 mL MeOH was added dropwise to a stirring 30 mL EtOH solution of [(L3)Na]Br (0.667 g, 1.22 mmol), and the reaction mixture was stirred at 60 °C overnight. Upon cooling, a small amount of white precipitate was filtered off. The filtrate was concentrated on a rotary evaporator, yielding a whitish-orange powder. This powder was then dissolved in a minimum amount (10 mL) of EtOH and this solution was added to a 10 mL EtOH solution saturated with NH_4PF_6. A very pale orange powder immediately precipitated, which was collected by vacuum filtration and washed with Et_2O to yield **3** (0.406 g, 0.502 mmol, 41% yield). Single crystals suitable for single-crystal X-ray diffraction were grown by vapor diffusion of Et_2O into a concentrated MeCN solution of **3**. Combustion analysis, calculated for $C_{24}H_{34}N_4O_4MnF_{12}P_2$: 36.61%C, 4.35%H, 7.11% N; found: 36.54%C, 4.37%H, 6.99%N. IR (cm^{-1}, diamond ATR): 2962, 2898, 2857, 1599, 1578, 1468, 1439, 1264, 1243, 1177, 1131, 1088, 1058, 1040, 1012, 939, 908, 878, 830, 782, 739, 719, 649, 556, 434, 407. LC-MS (*m*/*z*), positive ion mode: $\{[Mn(L3)]PF_6\}^+$, 642.16. See Fig. S3 for UV-Vis characterization and Fig. S18 for comparison of powder diffraction data with simulations from single-crystal analysis.

Single-crystal X-ray diffraction measurements

Single-crystal X-ray diffraction data for **1** and **2** were collected at the X-Ray Diffraction Facility of the Analytical Resources Core at Colorado State University. Data were collected on a Bruker D8 Quest ECO single-crystal X-ray diffractometer equipped with Mo Kα (λ = 0.71073 Å). Data for **3** were collected at the Crystallographic Facility at The Ohio State University. Experiments were performed with a Bruker Kappa Photon III CPAD diffractometer also equipped with Mo K_α radiation (λ = 0.71073 Å). Data were collected in a nitrogen gas stream at 100 (2) K using ϕ and ϖ scans for all species.

The collected data were integrated using the Bruker SAINT software program and scaled using the SADABS software program,[23] as implemented in Apex 4 software. Space group assignments were determined by examination of systematic absences, *E*-statistics, and successive refinement of the structures. Crystal structures were solved using SHELXT[24] and refined with the aid of successive difference Fourier maps by SHELXL[25,26] operated in conjunction with OLEX2 software.[27] None of the crystals demonstrated decay by X-ray radiation over the course of the experiment. All non-hydrogen atoms were refined anisotropically. Hydrogen atoms were placed in ideal positions and refined using a riding model for all structures. The structure of **1** was twinned, which we accounted for with a generic racemic TWIN matrix (−1 0 0 0 −1 0 0 0 −1) and refinement. Crystallographic data are summarized in the SI (Tables S1–S3) and the structures were deposited in the CSD under accession numbers 2215554 (**1**), 2215553 (**2**), and 2380186 (**3**). H-bond analysis was performed with Mercury (Table S4).[28]

Magnetic susceptibility and heat capacity measurements

Magnetic measurements were performed on polycrystalline samples of **1–3** using a Magnetic Property Measurement System MPMS3 (Quantum Design) equipped with a superconducting quantum interference device (SQUID) magnetometer MPMS3. Direct-current (DC) magnetic susceptibility was measured under an applied magnetic field of 1000 Oe in the 2–300 K temperature range, with a temperature sweep rate of 2 K min^{-1}. The data were corrected for the diamagnetic contribution from the sample holder and for the intrinsic diamagnetism by using Pascal's constants.[29]

Heat capacity measurements were performed on single crystal samples of **1–3** mounted in Apiezon N Grease using a Physical Property Measurement System DynaCool (Quantum Design) equipped with a single two-stage pulse tube cooler. Heat capacity was measured under applied magnetic fields of 0, 1, and 2 T in the 2–50 K temperature range using a 1% temperature rise. The data were corrected for the heat capacity contribution from the grease. See the SI for the equation and fitting details.

EPR measurements and analyses

Variable-field (up to 17 T) and high-frequency (390 GHz) EPR spectra were recorded with a home-built spectrometer at the EMR Facility of the National High Magnetic Field Laboratory in Tallahassee, FL. The instrument has been described in detail elsewhere.[30] Briefly, the instrument is a transmission-type device in which waves are propagated in cylindrical light pipes. The microwaves were generated by a phase-locked oscillator (Virginia Diodes) operating at a frequency of 8–20 GHz and generating its harmonics, of which the 4th, 8th, 12th, 16th, 24th and 32nd harmonics were available. A superconducting magnet (Oxford Instruments) capable of reaching a field of 17 T was employed. 390 GHz was selected as the frequency for EPR analysis based on signal-to-noise and peak-to-peak separation. Pulsed Q-band spectra were collected at the Ohio Advanced EPR Laboratory of Miami University (epr.muohio.edu) with a Bruker E 580 Q-band spectrometer using a dielectric resonator (EN 5107D2) and a Flexline cryostat with Oxford ITC. The general Hahn-echo pulse sequence used for collection of the echo-detected, field-swept spectrum used 10 ns π/2 and 20 ns π

pulses with 200 ns interpulse spacing. Microwave powers used during these experiments were adjusted to control echo size and prevent saturating the detector.

Samples for X-band EPR analyses of **1–3** were prepared by loading solutions of **1–3** in butyronitrile (5 mM) into a 4 mm outer diameter (OD) quartz EPR tube (Wilmad 707-SQ-250M) and placed into a Bruker ELEXSYS ESR-500 X-band EPR spectrometer (Bruker Biospin, Rheinstetten, Germany) for measurement. The high-sensitivity probe was used and temperatures were controlled *via* a Coldedge system for these measurements. Samples for Q-band EPR analyses of **2** were prepared by loading liquid solution (5 mM conc.) into 1.6 mm OD quartz capillaries. Samples for 390 GHz experiments were also solid, microcrystalline powders of **1**, **2**, and **3** dispersed in sucrose (as a general, EPR-inactive solid). However, for the high-field instrument, these powders were loaded into a plastic sample cup, not quartz, and inserted into the spectrometer. Sucrose was used for 390 GHz measurements to improve spectral quality and avoid saturating the detectors.

All EPR spectra were analyzed *via* the program Easyspin[31] and modeled by the spin Hamiltonian and broadening mechanisms reported in the main text and Tables S5–S10. For simulating these spectra, we started with the minimal number of parameters: isotropic g, D, and E, a careful eye to ensure $|E| \leq |D/3|$, and a minimal broadening model. We then stepwise added in parameters and inspected whether the expanded set provided a significantly better simulation. This approach led to the models in the report. Note that our simulations were also not conclusive of the signs of D and E. The shape of the simulated spectra would change dramatically with the signs of D and E. But, for all cases, tweaking of the g values for consistency with the signs of D and E (*e.g.* swapping g_x and g_y when flipping the sign of E) and subsequent adjustment to the broadening model could produce simulations with peaks that match the field positions of the peaks in the experimental data. We also attempted modelling the spectral broadening using D strain, but in our analyses, g strain provided far superior simulations.

Other physical measurements

Infrared spectra were recorded on a Bruker TENSOR II FTIR spectrometer. Mass spectrometry analyses were performed on an Agilent 6224 Accurate Mass TOF LC/MS in positive ion mode using direct injection. Peak assignment was based on m/z, interpeak spacing, and isotopic distribution. UV-Vis spectra were collected on solutions of complexes with a Shimadzu UV-2600i UV-Vis-NIR spectrophotometer and standard quartz cuvettes of 1 cm path length. Emission spectra were obtained on an Edinburgh FS5 spectrofluorometer using a quartz cuvette with a 1 cm path length in a temperature-controlled sample holder. Samples were prepared as 3.7, 11.7, and 0.23 mM solutions (**1**, **2**, and **3**, respectively) in MeCN and held at 20 °C. Steady state emission spectra were obtained by exciting each sample at 330 nm (**1** and **3**) and 220 nm (**2**) with a 5.0 nm slit width and spectral data were collected from 350 to 750 nm (**1** and **3**) and 240 to 650 nm (**2**). Spectra were averaged over three scans with a 0.5 s integration time. Powder X-ray diffraction data were obtained using a Bruker D8 Advance diffractometer (sealed Cu X-ray tube, 40 kV and 40 mA) equipped with a Lynxeye XE-T position-sensitive detector. The data were collected with an incident beam monochromator (Johansson type SiO_2 crystal) that selects only Cu Kα1 radiation (λ = 1.5418 Å) with a scan rate of 3° min^{-1} at 293 K with an exposure time of 0.5 and 1 seconds.

Results and discussion

Synthesis of the studied complexes proceeded by combining either the encapsulating ligands (**1** and **2**) or the NaBr adduct of the ligand (**3**) with $MnCl_2$ in ethanol (Scheme 1). Owing to the challenges in the crystallization of these halide salts, we used $(NH_4)[PF_6]$ for counterion metathesis reactions that yielded the PF_6^- salts of **1**, **2**, and **3** as yellow-orange compounds. These compounds were readily crystallized for single-crystal X-ray diffraction analyses (Tables S1–S3).

The Mn(II) ions in complexes **1–3** are of varying geometry (Fig. 1). For **1** and **2**, the Mn ions are six-coordinate, bound to the side arms of the cryptand ligands, and the apical N atoms are unbound, though seemingly oriented with the lone pair pointing toward the Mn ion. For **3**, the Mn ion is eight-coordinate, bound to four N and four O atoms of the ligand. For **1**, average Mn–N distances are 2.30(3) Å for bound N atoms and 3.12(8) Å for the apical N atoms. For **2**, the Mn–N distances expand slightly to 2.443(1) Å for bound N atoms but contract slightly to 2.85(5) Å for the apical N–Mn distance. This structural change likely reflects the change in the metal–ligand interaction for *imino* N-donor atoms *versus* the *amino* N-donor atoms, which then distorts the total ligand geometry and shifts the apical N atoms. For **3**, there are two sets of Mn–N bonds, one set with the bipyridine group and the other with tertiary amines, with average Mn–N distances of 2.27(1) and 2.44(7) Å, respectively. For **3**, there are also four Mn–O bonds, with an average distance of 2.40(5) Å. The local geometries of the Mn(II) ions in **1** and **2** are best described as axially com-

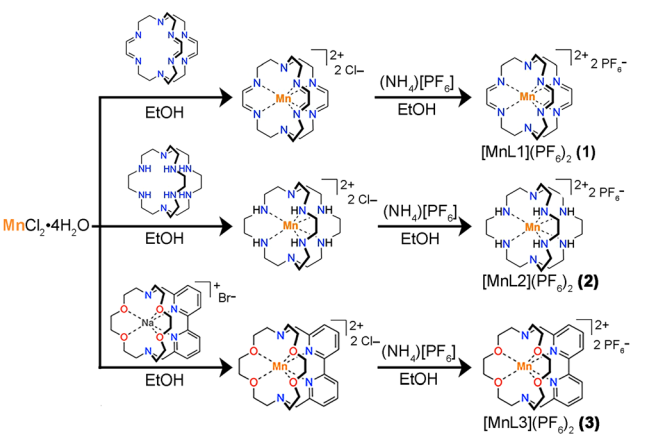

Scheme 1 Synthetic routes to complexes **1–3**.

pressed trigonal antiprismatic geometries, as the N–Mn–N bite angles are 71.92(3)° for **1** and 71.6(1)° for **2** (Fig. S1). In contrast, the Mn(II) geometry in **3** is a distorted dodecahedral/square antiprismatic one, owing to the larger coordination number and three distinct types of donor atoms. Finally, the structure of **2** features NH bonds in the coordination sphere of Mn(II) oriented toward the closest PF_6^- anion (Fig. S2) with NH···FPF_5^- distances of *ca.* 2.35 Å, suggesting that hydrogen bonding interactions are present in the crystalline phase.[32] These same contacts are absent in the structures of **1** and **3** (see Table S4).

Solution phase UV-Vis spectroscopy measurements of **1–3** reveal peaks above 20 000 cm^{-1} with strong intensities indicative of charge-transfer bands (Fig. S3). Complex **1** exhibits the lowest energy peak of the series, near 29 000 cm^{-1}. Complex **3** yields the next lowest energy peaks, near 33 000 and 40 000 cm^{-1}. Complex **2** yields the highest energy peak, near 45 000 cm^{-1}. The energies and intensities of these transitions suggest that they are charge-transfer transitions, and the extended conjugated units for **1** and **3** suggest assignment as metal-to-ligand charge transfer. For **2**, however, which has no extended conjugation on the ligand shell, assignment of the high-energy transition is not as clear. We can say, at least initially, that this transition is probably not an exceptionally high-energy d–d transition. Indeed, a d–d transition in the trigonally-compressed D_{3d} geometry is forbidden by the Laporte selection rule. Furthermore, if the peak for **2** were a simple d–d transition, then the peak would suggest a stronger ligand field for **2** than systems with extremely strong-field ligands, like $[Mn(CN\text{-}B(C_6F_5)_3)_6]^{4-}$,[33] which we think is unlikely for the hexamine nature of the ligand shell in **2**. In any case, outside this one peak, the spectra are within expectation for Mn(II) as a high-spin, high-coordinate ion with a half-filled shell, where any d–d transitions are forbidden and weak or not observed.[34]

Complexes **1–3** also emit light when irradiated with light in the 300–220 nm window (Fig. S4). The trend in the highest emission intensity follows from **1** to **2** to **3**. Complex **1** emits at 21 300 cm^{-1}, **3** emits at 30 800 cm^{-1}, and then **2** yields even higher-energy emission, near 37 000 cm^{-1}. The ground state of the Mn(II) ions in **1–3** is $^6A_1$, as indicated by the $S = 5/2$ ground state (see magnetic analyses below). Inspection of the d^5 Tanabe–Sugano diagram[35] with the $^6A_1$ ground state in mind suggests that the trend in emission energy could reflect a decreasing ligand-field strength across the ligand shell if the observed emission is from any of the lowest-three energy excited states ($^4T_2$, $^4T_1$, or $^2T_2$), with the $^2T_2 \rightarrow {}^6A_1$ emission being lowest in energy. These emissive characteristics are in agreement with observations for other molecular Mn(II) complexes.[36,37]

Potential correlation of the electronic structures of **1–3** with zero-field splitting and other spin-Hamiltonian parameters was pursued using magnetic susceptibility and two EPR techniques. At 300 K, $\chi_M T$ values for **1**, **2**, and **3** were, respectively, 4.02, 4.28 and 4.32 cm^3 K mol^{-1} (Fig. S5). These values are close to the expected room temperature value of 4.38 cm^3 K mol^{-1} for $S = 5/2$ and $g = 2.00$. With decreasing temperature, $\chi_M T$ is relatively constant with little temperature dependence. Zero-field splitting values larger than *ca.* 1 cm^{-1} will produce T-dependent $\chi_M T$ values below 50 K; hence, the absence of a strong T-dependence highlights a very small zero-field splitting (<1 cm^{-1}).

The first EPR analysis we pursued was low-temperature (5 K), high-frequency (390 GHz), high-field EPR spectroscopy in the solid state (Fig. 2) to provide the best resolution of D. At high field and for most Mn(II) species (which often have positive D values < *ca.* 1 cm^{-1}), the EPR experiment proceeds in the so-called high-field limit, where the Zeeman interaction is the largest-energy term in the spin-Hamiltonian. As a result, one should expect five peaks corresponding to $|M_S = -5/2\rangle$ to $|M_S = -3/2\rangle$, $|M_S = -3/2\rangle$ to $|M_S = -1/2\rangle$, $|M_S = -1/2\rangle$ to $|M_S = +1/2\rangle$, $|M_S = +1/2\rangle$ to $|M_S = +3/2\rangle$, and $|M_S = +3/2\rangle$ to $|M_S = +5/2\rangle$ transitions. The resolution of these individual peaks at high frequency may be challenging owing to broadening from the D or g strain and unresolved hyperfine interactions (*e.g.* with $I = 5/2$ ^{55}Mn or $I = 1$ ^{14}N and $I = 1/2$ ^{15}N donor atoms).[38] Nevertheless, the span of the peaks on the field axis should trend with the zero-field splitting magnitude for Mn(II) and display a greater width for a larger D magnitude.

Simulations of the 390 GHz EPR spectra for **1–3** at 5 K (Fig. 2) give a general trend in the zero-field splitting magnitude of $|D|$ increasing from **1** to **2** to **3**. These values were determined from Easyspin,[31] which modeled the spectra using the following spin Hamiltonian:

$$\hat{H} = \mu_B \boldsymbol{B} \cdot \boldsymbol{g} \cdot \boldsymbol{S} + D\hat{S}_z^2 + E(\hat{S}_x^2 - \hat{S}_y^2)$$

Here, μ_B is the Bohr magneton, $\boldsymbol{g}$ is the anisotropic $\boldsymbol{g}$ factor, $\boldsymbol{S}$ and $\boldsymbol{B}$ are the spin and magnetic field, respectively, D is the

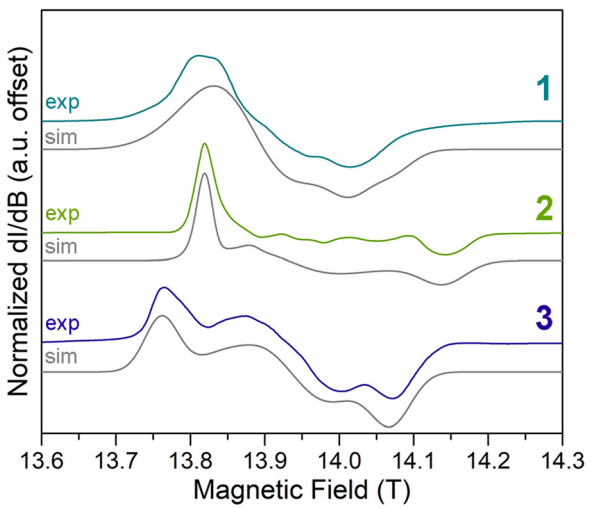

Fig. 2 5 K 390 GHz EPR spectra for **1–3**. Spectra were collected on sucrose dispersions. Solid gray lines are simulations using the following spin-Hamiltonian parameters: for **1**, $g_x = 2.008$, $g_y = 2.000$, $g_z = 2.004$, $D = +800$ MHz, $E = +220$ MHz; for **2**, $g_x = 1.998$, $g_y = 1.999$, $g_z = 1.989$, $D = +900$ MHz, $E = 220$ MHz; for **3**, $g_x = 1.997$, $g_y = 2.006$, $g_z = 2.001$, $D = +1050$ MHz, $E = +260$ MHz. See the SI for additional details.

axial zero-field splitting, E is the transverse zero-field splitting, and $\hat{S}_i^2$ ($i = x, y$, and z) are the spin operators.

There are several important details regarding the simulations to mention here. First, none of the 390 GHz spectra depict a clear six-line splitting that can be attributed to hyperfine coupling between the $S = 5/2$ electronic spin and the $I = 5/2$ ^{55}Mn nucleus, and it is likely that the hyperfine coupling is contained within the general broadening of the spectra we observe (see the SI for simulation details). Hence, we specifically avoid the inclusion of hyperfine coupling because of the spectral absence of its effects and a desire to avoid overparameterization. Second, simulations of the spectra often had two solutions, one with positive D and E and one with negative D and E. Hence, the signs of D and E are likely not well resolved in these species (Fig. S6). The Mn(II) ion generally produces D values that are greater than zero,[39,40] and hence we tentatively assume that complexes **1**–**3** are consistent with that broader picture, though our spectra are themselves inconclusive of the sign. The best simulations are depicted in Fig. 2. The obtained values of D and E are, respectively, $|D|$ = 800 and $|E|$ = 220 MHz for **1**, $|D|$ = 900 and $|E|$ = 220 MHz for **2**, and $|D|$ = 1050 and $|E|$ = 260 MHz for **3**. The g values for all three are rhombic, with average values of 2.004, 1.995, and 2.001, respectively, for **1**, **2**, and **3**. All fitting parameters are reported in the SI (Tables S5–S7). Finally, note that at high field/frequency, broadening of the spectra because of inhomogeneity in the g values (g strain) is a potential convoluting factor in spectral simulation and the temperature dependence (*vide infra*). For all compounds, however, adjustments of the strain failed to account for the changing spectral shapes at low temperatures, acutely so for **2**.

The general magnitudes of D obtained here are consistent with expectations for the Mn(II) ion and our other magnetic data.[41–44] Indeed, the observed temperature independence of the $\chi_M T$ data suggests $|D| < 1$ cm^{-1}. The obtained signs of D and E are also consistent with the general expectations for $S = 5/2$, Mn(II).[39,45,46] Furthermore, our use of MHz as an energy unit here is necessitated by the small magnitudes in D and E that we observe; for ease of comparison with other transition metal ions, wherein D and E are often much larger,[11] note that 29 979 MHz = 1 cm^{-1}. The UV-Vis data suggest that most electronic states for the Mn(II) ions in **1**–**3** are high energy relative to the ground state. The inverse relationship between the zero-field splitting value and the energy separation between the ground and excited states suggests that these contributions should be small and consistent with the small D values we find here.

Next, we evaluated the temperature dependence of the EPR spectra for evidence of ligand effects on the temperature sensitivity of D and E. For **1**, **2**, and **3**, the 390 GHz EPR spectra from 5 to 300 K reveal broad signals near $g = 2.00$ (13.9 T) with an overall width that varies with temperature in a unique way for each complex (Fig. 3). For **1**, the width of the signal (peak-to-peak) is *ca.* 0.07 T at 300 K and widens slightly with decreasing temperature, but more dramatically below 30 K to 0.2 T at 5 K. For **2**, in contrast, the spectral width starts at 0.36 T at

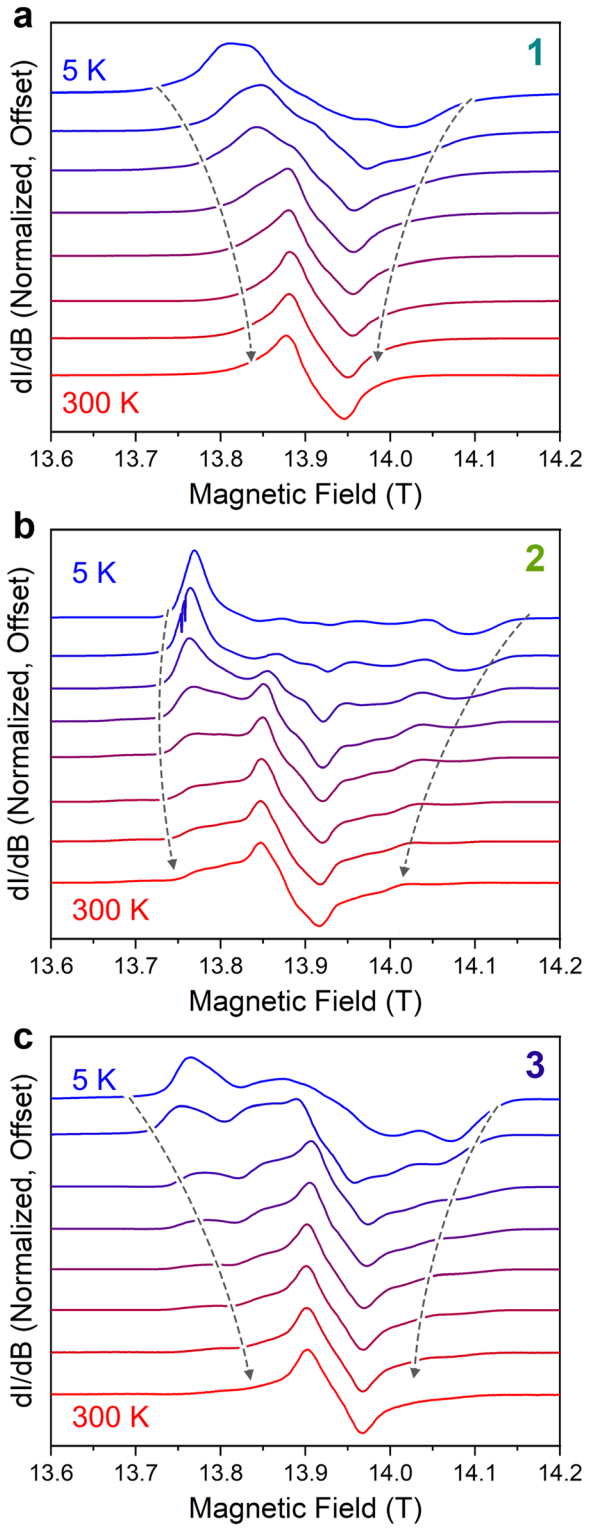

Fig. 3 Select variable-temperature, high-frequency EPR spectra. (a) Temperature dependence for **1**. (b) Temperature dependence for **2**. (c) Temperature dependence for **3**. All spectra were collected from 5 to 300 K at 390 GHz on pure compounds dispersed in sucrose. Spectra vary in width across this range as a result of the temperature sensitivity of the zero-field splitting. Dashed grey lines are guides to the eye to illustrate the collapse of spectral width.

300 K and decreases by only 0.04 T from 300 to 5 K. Finally, for **3**, the spectral width increases with decreasing temperature, from 0.07 T at 300 K to 0.3 T at 5 K. The shapes of the spectra change as well, in some cases appearing to be single, broad resonances with slight features to the low/high field of the main peak. At low temperature, however, the shapes are far more distinct.

The broadness and shapes of the collected 390 GHz variable-temperature spectra were modeled with the program Easyspin[31] to extract g, D, and E values for the studied complexes and their temperature dependence (Fig. S7–S9 and Tables S5–S7). For all complexes, g values hover close to 2.00 from 5 to 300 K with slight anisotropy that varies slightly with temperature. The obtained D and E values vary in a more noticeable way with temperature (Fig. 4). For **1**, D is 650 MHz at 300 K and increases slowly and only slightly with decreasing temperature to 700 MHz at 30 K. Below 30 K, D for **1** increases more substantially, reaching 800 MHz at 5 K. For **2**, D is relatively constant near 1300 MHz from 300 to 40 K but decreases below 40 K to 900 MHz at 5 K. Finally, for **3**, D increases slightly from 900 to 940 MHz from 300 to 20 K, then more drastically, reaching 1050 MHz at 5 K. It is interesting that the relative ranking of D values is generally **2** (1300 MHz) > **3** (900 MHz) > **1** (650 MHz), except at the lowest temperatures of analysis. The obtained E values are smaller than the D values and exhibit smaller T sensitivity, showing the highest changes below 30 K, like D, but generally reflect the trends in D (*i.e.* E of **3** > E of **2** > E of **1**). We also note that some of the spectral changes may stem from changes in relaxation times for the observed transitions, which are known to have temperature dependence.[10,47] The effects of these times are therefore likely reflected in the temperature dependence of the strain parameters (see Tables S5–S7).

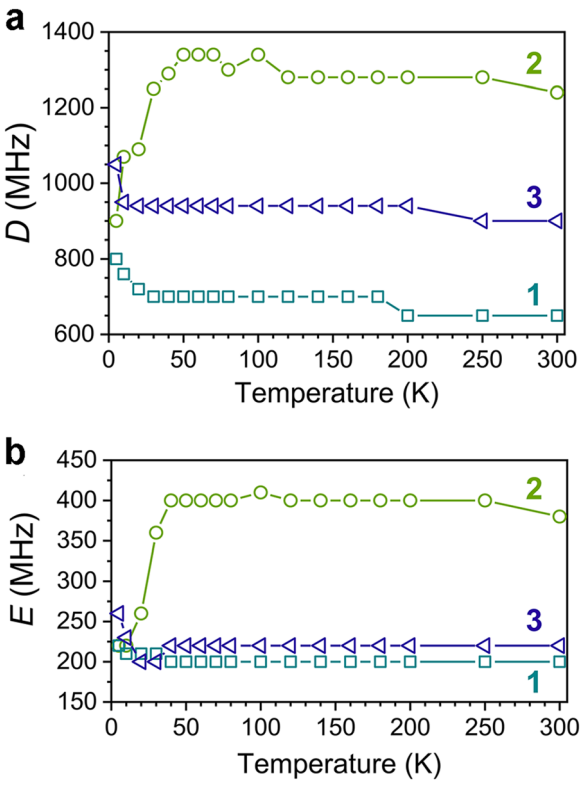

Fig. 4 Temperature dependence of D and E in the solid state, 390 GHz analyses of **1**, **2**, and **3**. (a) Temperature dependence of D values. The uncertainty in each D value is *ca.* 10 MHz and evaluated by the eye. (b) Temperature dependence of the E values for **1**, **2**, and **3**. Uncertainties in E are *ca.* 20 MHz. Solid lines in both a and b are guides to the eye.

The apparent temperature sensitivities of the zero-field splitting are large. Taking the change in D for **1**, **2**, and **3** over the temperature range of 5 to 50 K, one finds 2.2, 9.8, and 2.2 MHz K^{-1} for the temperature sensitivity of D. For E, the temperature sensitivities are generally smaller over this window. For **1**, **2**, and **3**, $\Delta E/\Delta T$ values are 0.4, 4, and 0.9 MHz K^{-1}, respectively. At higher temperatures, the changes are much smaller. From 50 to 300 K, $\Delta D/\Delta T$ values are 0.2, 0.4, and 0.2 MHz K^{-1}, respectively, and $\Delta E/\Delta T$ values are 0, 0.1, and 0 MHz K^{-1} for **1**, **2**, and **3**, respectively. These values are significant in the broader picture of temperature-dependent zero-field splittings. The temperature-dependent values of D and E that we observe are, except for the $\Delta E/\Delta T$ values of **1** and **3**, all greater than the temperature sensitivity of the D value of the S = 1 NV center in a diamond lattice (−74.2(7) kHz K^{-1}),[18,19] by several orders of magnitude. These values are also among the highest temperature sensitivities for molecular systems and eclipse those of several other notable molecules. For example, the $\Delta D/\Delta T$ value of **2** eclipses the 5.7 MHz K^{-1} dependence on the singlet–triplet EPR transition in $[Cu_2(tren)_2(OCN)_2](BPh_4)_2$ (tren = 2,2′,2″-triaminotriethylamine),[48] 2.4 MHz K^{-1} sensitivity for the S = 5/2 $[Fe(DMSO)_6](NO_3)_3$,[49] 2.3 MHz K^{-1} sensitivity for $[Cr(en)_3]^{3+}$ doped with $[Co(en)_3]Cl_3{\cdot}0.5NaCl{\cdot}3H_2O$,[50] and 1.5 MHz K^{-1} sensitivity for $[Cr(H_2O)_6]^{3+}$ in guanidinium aluminum sulfate hexahydrate.[51] The only compound that **2** is second to is an S = 1 ferromagnetic dicopper complex where $\Delta D/\Delta T$ is *ca.* 16 MHz K^{-1}.[52] Importantly, though our system moves the bar higher for mononuclear systems, all of these examples are orders of magnitude higher than the NV center. We propose that the aggregate of these results underlines the promise of molecular systems in this space, as this class of structures likely exhibits greater flexibility with changes in temperature than the rigid diamond lattice. Finally, we note that the temperature sensitivity here also eclipses the highest sensitivity of any known nuclear spin, 18 kHz K^{-1}, found in the spin-crossover-active trinuclear Co(III) complex $[(CpCo(OP(OR)_2)_3)_2Co]^+$.[53]

We also applied X-band EPR spectroscopy to frozen solutions of **1–3** in butyronitrile, a solvent that glasses when frozen (Fig. 5 and S10). We hypothesized that the lower frequency may sharpen spectra sufficiently to enable the observation of hyperfine coupling (and any associated temperature dependence),[38] as well as provide a second estimate of the T-dependence of the zero-field splitting in a different phase than microcrystalline powder. The X-band EPR spectra for **1–3** exhibit intense peaks at *ca.* 3500 G with smaller features in lower and higher fields, as is typical of low-zero-field splitting

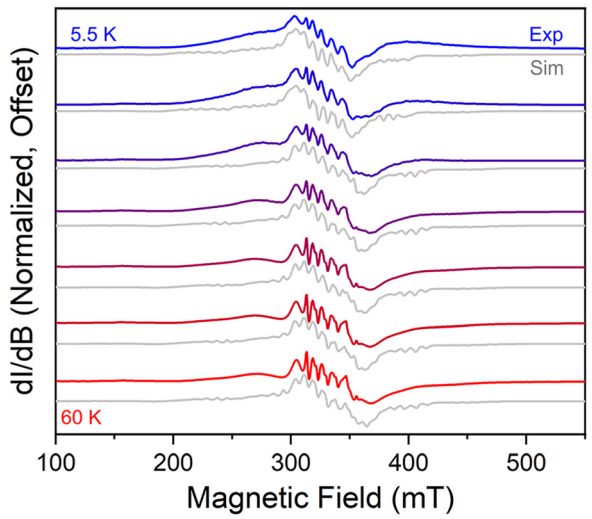

Fig. 5 Variable-temperature EPR spectra of complex **2** collected from 5.5 K to 60 K at 9.3 GHz in 5 mM butyronitrile solutions. Colored lines are the experimental data and the gray lines are spectral simulations. Spin-Hamiltonian parameters can be found in Table S8.

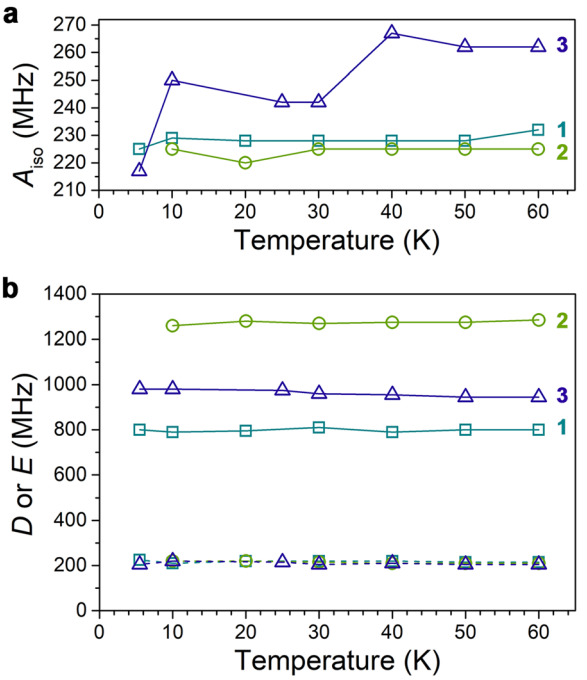

Fig. 6 Temperature dependence of the spin Hamiltonian parameters of **1–3** in frozen butyronitrile solutions. Measurements were performed at 9.3 GHz frequency. (a) Temperature dependence of isotropic *A* values. Uncertainties, as evaluated by the eye, are on the order of 10 MHz. (b) Temperature dependence of *D* values (connected by solid lines) and *E* values (connected by dashed lines). The uncertainties in the *D* values are *ca.* 5 MHz and the uncertainties in *E* are *ca.* 10 MHz. Solid/dashed lines in both a and b are guides to the eye.

(*e.g.* Mn(II)) complexes. Importantly, the strongest central peak and some of the minor peaks exhibit the six-fold pattern that is typical of Mn(II) with hyperfine coupling to the $I = 5/2$ ^{55}Mn nucleus. At temperatures below 30 K, there were noticeable changes between each temperature point, because small spectral features sharpened with decreasing temperature for all species. A growth in spectral tails away from the central feature near 400 and 280 mT is evident at lower temperatures, though the field position stays relatively constant until those features broaden into the central signal at the lowest temperatures. Beyond those changes, only very slight changes appear to the rest of the peak positions, suggesting that *g* and *A* vary weakly with temperature for **1–3** in frozen solution.

To quantify these temperature dependences (or lack thereof), spectral simulations of the frozen-solution spectra were carried out in EasySpin.[31] The spin-Hamiltonian parameters from the best simulations are listed in Tables S8–S10. Note that the lower-frequency experiment afforded a sharper spectrum with clear hyperfine peaks (relative to the high-frequency data); therefore, we used a spin Hamiltonian augmented with that interaction:

$$\hat{H} = \mu_B \boldsymbol{B} \cdot \boldsymbol{g} \cdot \boldsymbol{S} + D\hat{S}_z^{\,2} + E(\hat{S}_x^{\,2} - \hat{S}_y^{\,2}) + \hat{\boldsymbol{S}} \cdot \boldsymbol{A} \cdot \hat{\boldsymbol{I}}$$

Here, all the terms have the same definition as in the spin Hamiltonian used to simulate the crystalline-state data, but now there is a nuclear spin operator ($\hat{\mathbf{I}}$) and the electronuclear hyperfine interaction (**A**).

The values of the spin Hamiltonian parameters for **1–3** vary slightly in the frozen solution analyses as a function of complex and temperature (Fig. 6). For example, the obtained values for g_x, g_y, and g_z are all near 2.00 for **1–3** at all temperatures (with slight variations). The *A* magnitude ranges from 210 to 240 MHz depending on the component (A_x *vs.* A_y *vs.* A_z) for **1–2**, while the range in *A* for **3** is from 210 to 300 MHz. The *D* values extracted by the simulations are near 800 MHz for **1**, 1270 MHz for **2**, and 960 MHz for **3**, in general agreement with the trend observed in the solid state. The values of *E* for **1–3** in frozen solution are all *ca.* 210–215 MHz. These values are close to those collected in the solid state, except for **2**, which displayed a larger *E*, *ca.* 400 MHz, in crystalline form.

The temperature sensitivities of the spin-Hamiltonian parameters are all small in frozen solution relative to the crystalline state. The *g* values are relatively temperature insensitive, varying slightly over the measured range. As a function of temperature, the average *A* value slightly increases for **1**, from 225 to 231 MHz, does not change for **2**, and increases from 217 to 262 MHz for **3**. For *A*, these temperature sensitivities are found to be *ca.* 0.8 MHz K^{-1}, much lower than the $\Delta D/\Delta T$ values seen in the solid state. The values of *D* also change but evidently do so substantially less than in the solid state. For **1**, *D* is nearly invariant at 800 MHz, as is *E*, the latter changing from 225 to 215 MHz from 5.5 to 60 K. For **2**, *D* increases slightly by 25 MHz over that same temperature range while *E* decreases by 10 MHz. Finally, for **3**, *D* drops by 35 MHz from 5.5 to 60 K and *E* is invariant at 205 MHz. These temperature sensitivities are all much lower than those collected in the solid state. Indeed, the highest sensitivity from these solution-phase studies, for *D* in **3**, is 0.6 MHz K^{-1}, an order of magni-

tude lower than the results in the microcrystalline state and lower than the frozen-solution $\Delta A/\Delta T$ parameters.

Note that changes in the molecular structure that affect the electronic structure of a metal could also impact the hyperfine coupling. For example, at a coarse level, small changes in M–L bond distances could adjust Mn–N covalency, which could impact the observed ^{55}Mn hyperfine coupling. That same structural change could also modify the spin–spin coupling of the Mn(II) ion as well as its excited state energies, both of which would influence the zero-field splitting. The lack of distinct changes in the hyperfine peak field positions with temperature, both for the central line and the outer transitions (see Fig. S11–S13), could potentially reflect a lack of temperature dependence of the spin Hamiltonian parameters for **1–3** in frozen solution. We performed additional measurements with Q-band pulsed EPR spectroscopy to test this interpretation by improving spectroscopic resolution and bridging the gap between the low- and high-frequency regimes of our analyses. We selected **2**, specifically, for these measurements since this complex showed the most dramatic change in D with T in the solid state. Echo-detected, field-swept spectra on solutions between 5 and 50 K (Fig. S14–15) reveal similar spectroscopic temperature-independence of the hyperfine transitions.

We note some specific cautions that should be taken in interpreting these data as concrete evidence of spin-Hamiltonian temperature independence. First, the potential influence of temperature-dependent changes in the molecular structure on hyperfine and zero-field splitting, while coarsely related to the structure, could offset or convolute one another, such that the peak T-independence does not directly disprove a temperature dependence of those parameters. Second, the frozen-solution spectra in Fig. 5 and S10–S15 are admittedly complicated at lower temperatures, which may be convoluting our interpretation, as perfect simulation is incredibly challenging to attain.

We performed variable-field, variable-temperature heat capacity measurements for **1–3** to test for a simple structural or magnetic phase transition as the origin of the temperature dependence of D (Fig. 7, S16 and S17). Data were collected on microcrystalline samples of **1–3** from temperatures of 50 to 2 K, the temperature range over which the largest EPR changes were seen, and magnetic fields of 0, 1 and 2 T. With decreasing temperature from 50 to 10 K, the heat capacities of **1–3** decrease slowly from *ca.* 20 to *ca.* 3 J mol^{-1} K^{-1} regardless of the applied magnetic field. Below 10 K, the heat capacities diverge, with a general ordering of $C_p(2\ T) > C_p(1\ T) > C_p(0\ T)$. Importantly, none of the compounds show a sharp peak in the heat capacity over the measured temperature range, ruling out a crystallographic phase transition as the source of the temperature-dependent spin Hamiltonian parameters. Furthermore, we did not see a sharp field-dependent transition either, suggesting no magnetic phase transition as the origin of the temperature dependence.

The field and temperature dependence of the heat capacities of **1–3** likely reflects the individual temperature-dependent contributions from the lattice and spin systems

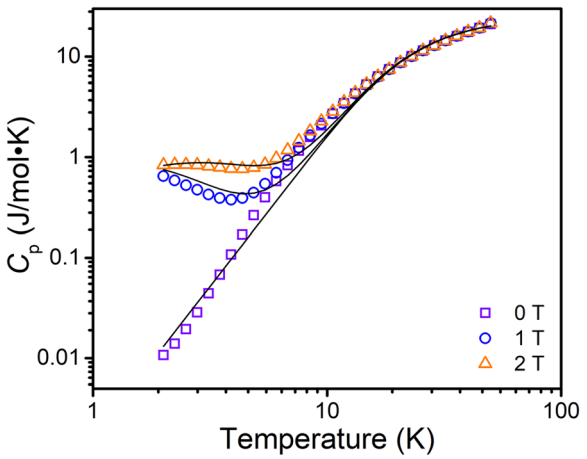

Fig. 7 Field and temperature-dependence of the heat capacity of **1** measured from 2 to 50 K. Solid lines are simulations of the heat capacity; see the main text for details.

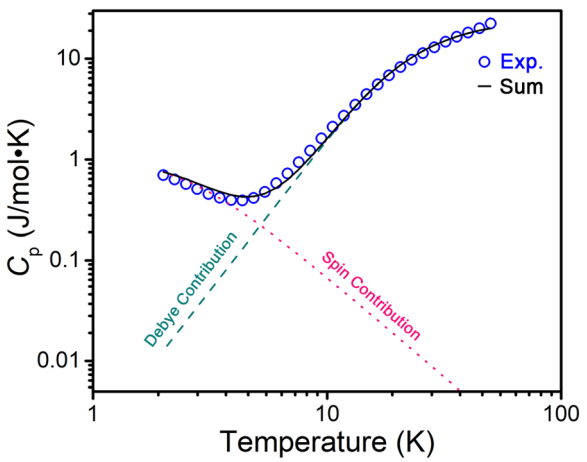

Fig. 8 Representative depiction of the two competing contributions to the heat capacity data in **1–3**. Here we show data collected for **2** under an applied magnetic field of 1 T.

(see Fig. 8 for **2** as a representative case). The curvature of the heat capacity at higher temperatures likely stems from the lattice itself (the Debye contribution), which can be found in diamagnetic complexes that are close in size to **1–3**.[54] At lower temperatures, both the increase in C_p with increasing magnetic field and the increase in C_p with decreasing temperature (at $B \neq 0$ T) reflect the magnetic contribution. For Mn(II), there may be two potential origins of this effect:[55] either the zero-field splitting of the $S = 5/2$ moment and/or the hyperfine coupling of that $S = 5/2$ spin with the $I = 5/2$ ^{55}Mn nucleus. Discerning between the contributions of these two factors is a challenge, because the energy scales of the zero-field splittings here (*ca.* 700–1400 MHz for D and *ca.* 300 MHz for E) are close to the hyperfine coupling interactions (*ca.* 200 MHz in **1–3**).

We simulated the heat capacities of **1–3** trying to account for all the above contributions to the heat capacity (Fig. 7, 8,

S16 and S17). We note that we were able to simulate the heat capacities far better using just the Debye and zero-field splitting contributions than including the hyperfine interaction, which typically contributes most to the heat capacity below 1 K, beyond our measurement window.[56] Hence, we restricted our simulations to just the Debye contribution and zero-field splitting interaction for a minimal effective model. The extracted g, D, and E values are relatively close for all complexes: 2.2 for g, 26 MHz for D, and 3 MHz for E for **1**, 2.2 for g, 31 MHz for D and 3 MHz for E for **2**, and 2.2 for g, 31 MHz for D and 3 MHz for E for **3**. Debye temperatures (θ_d) for **1–3** were 105(1), 107(1) and 97(1) K, respectively, close to the values for other salts of mononuclear metal complexes.[54] The g, D, and E values obtained here are significantly different from the EPR values and likely have substantial relative uncertainties given the small values. We propose that higher confidence should be placed in the values obtained from EPR measurements because EPR is a resonant technique, *versus* heat capacity measurement values that are obtained in bulk solids. Similar disagreements in spin Hamiltonian values between EPR and magnetic susceptibility are often found for similar reasons,[57,58] and here the effect may be amplified by the generally lower values of D and E relative to the full temperature range of the experiments. Nevertheless, the heat capacity data agree with the conclusion that D and E are small relative to many other transition metals[11] for **1–3**.

The collected data allow two distinct and tentative interpretations of the temperature sensitivity of the EPR spectra. First, we see large temperature sensitivities in the spin Hamiltonian parameters of these complexes that appear in the solid state, not in solution. This variation in sensitivity could be evidence of the importance of complex–counterion interactions in dictating the temperature dependence. Second, we see no sharp features in the heat capacities, so we can rule out crystallographic transitions as a driving effect. So, we may be seeing that PF_6^-–complex interactions are guiding the small, temperature-dependent changes in bond lengths and angles which affect D and the other parameters. This argument is akin to the rationale for temperature dependence of ^{59}Co NMR parameters,[15] and it should be noted that ^{59}Co NMR parameters and EPR parameters[11] both ultimately stem from the electronic/physical structures of the coordination shell. If this is true, we speculate that the "turning on" of the effect at the lowest temperatures could be supporting selective population of only select low-energy modes.

A second interpretation of the spectral changes relates to increasing spin populations of the $M_S = -5/2$ levels rather than changes in D. For the $S = 5/2$ Mn(II) ion at high magnetic field/microwave frequency, $\Delta M_S = 1$ transitions from the ground $M_S = -5/2$ level exhibit the highest anisotropy and broadening in the powder EPR spectrum relative to the others. In this system at high temperature, where all M_S levels are populated, the sharpest transition would most likely be the central one between the $M_S = \pm\frac{1}{2}$ levels. In this interpretation, a decreasing temperature could trigger an apparent signal broadening *via* growth in the population of the ground −5/2 level and its transitions. This mechanism would be independent of a change in D and would be consistent with (1) the observation of maximum signal change at the lowest temperatures of the solid-state measurements, (2) the lack of observation of temperature dependence in the solution-phase measurements, which were collected at relatively high temperatures, and (3) the lack of a phase transition in the heat-capacity measurements. This interpretation does not, however, enable a straightforward description of what differentiates **1–3**. Future experiments will ultimately be necessary to disprove either of the two mechanisms.

Finally, we think these data are an important note of caution for drawing structure–property relationships in systems with relatively small-magnitude spin-Hamiltonian parameters. Low-temperature high-field/frequency EPR measurements are often performed to determine the signs of D and E for high-spin complexes, though we did not need to apply that analysis here.[14] We think these data urge caution in comparing D values that are close between similar complexes, particularly if the temperatures of EPR and X-ray diffraction analyses are different. Indeed, we see that the general trend in D magnitude switches from **1** < **2** < **3** at the lowest temperatures to **1** < **3** < **2** at the highest. We emphasize that the importance of this caution is largest when the general magnitudes of D, g, E, *etc.* are relatively small, as they are here. For example, a compound with a D value greater than 5 cm^{-1} is likely to yield spectra attributable to a greater-than-5 cm^{-1} D-value complex at all temperatures, because even a 1000 MHz shift is relatively small compared to the total magnitude of D (1000 MHz ≈ 0.03 cm^{-1}). A complex with a *ca.* 500 MHz D value will, in contrast, yield vastly different spectra with the same 1000 MHz shift.

Conclusions

The foregoing data illustrate that Mn(II) complexes can exhibit highly temperature-dependent EPR spectra that eclipse the thermal sensitivity of the NV center. These temperature sensitivities could stem from temperature dependent zero-field splittings that are tunable by ligand selection. However, future studies will be necessary to fully elucidate the mechanisms of thermal sensitivity, whether driven by small M–L bond distances and angles or through the spectral influence of changes in spin polarizations. In the long term, the high apparent sensitivities could be applied to developing new molecular imaging thermometers *via* EPR imaging or optically detected magnetic resonance.

Author contributions

A. J. C., A. G., S. S., and S. D. executed the syntheses, basic characterization, and X-band EPR analysis. C. E. J., R. M., Ö. Ü., and A. O. performed the high field/frequency EPR analyses. A. G. and I. B. conducted the heat capacity measurements. J. M. Z., A. J. C.,

A. G., and S. S. conceived the experiments. All authors were involved in assembling the manuscript.

Conflicts of interest

There are no conflicts to declare.

Data availability

All data related to this article, including EPR spectra, magnetometry, heat capacity, UV-Vis, and powder diffraction data, can be found at the Dryad digital data repository at https://doi.org/10.5061/dryad.bcc2fqzpj. Any manuscript data not found in these two resources are available in the supplementary information (SI) of this article.

Supplementary information: full experimental details and additional crystallographic, magnetic, heat-capacity, and spectral data. See DOI: https://doi.org/10.1039/d5dt02920a.

CCDC 2215553, 2215554 and 2380186 for **1–3** contain the supplementary crystallographic data for this paper.[59a–c]

Acknowledgements

We thank Dr R. McCarrick for experimental assistance and thoughtful input. We also thank Prof. S. Hill for insightful discussions. This research was performed with the support of Colorado State University (CSU), The Ohio State University, and in part by the National Institutes of Health (R21-EB027293) and the Department of Energy (DE-SC0021259). Nuclear magnetic resonance experiments and standard molecular characterization were performed at the CSU Analytical Resources Core (Research Resource ID: SCR_021758), which is supported by an NIH-SIG award (1S10OD021814-01) and the CSU-CORES Program. A portion of this work was performed at the National High Magnetic Field Laboratory, which is supported by National Science Foundation Cooperative Agreement No. DMR-1644779 and the State of Florida. The pulsed Q-band EPR analyses were performed at the Ohio Advanced EPR Laboratory, which is supported in part by the NSF (MRI-1725502).

References

1 C.-J. Yu, S. von Kugelgen, D. W. Laorenza and D. E. Freedman, *ACS Cent. Sci.*, 2021, **7**, 712–723.
2 C. L. Degen, F. Reinhard and P. Cappellaro, *Rev. Mod. Phys.*, 2017, **89**, 035002.
3 J. P. Klare, *Biomed. Spectrosc. Imaging*, 2012, **1**, 101–124.
4 In Vivo EPR (ESR), ed. L. J. Berliner, Springer US, Boston, MA, 2003.
5 G. Kucsko, P. C. Maurer, N. Y. Yao, M. Kubo, H. J. Noh, P. K. Lo, H. Park and M. D. Lukin, *Nature*, 2013, **500**, 54–58.
6 R. Schirhagl, K. Chang, M. Loretz and C. L. Degen, *Annu. Rev. Phys. Chem.*, 2014, **65**, 83–105.
7 J. A. Real, A. B. Gaspar and M. C. Muñoz, *Dalton Trans.*, 2005, 2062–2079.
8 T. Tezgerevska, K. G. Alley and C. Boskovic, *Coord. Chem. Rev.*, 2014, **268**, 23–40.
9 R. T. Hitchcock, Radio-Frequency and Microwave Radiation, In *Patty's Toxicology*, ed. E. Bingham, B. Cohrssen and C. H. Powell, 2012, DOI: 10.1002/0471435139.tox101.pub2.
10 C. E. Jackson, I. P. Moseley, R. Martinez, S. Sung and J. Zadrozny, *Chem. Soc. Rev.*, 2021, **50**, 6684–6699.
11 S. Gómez-Coca, D. Aravena, R. Morales and E. Ruiz, *Coord. Chem. Rev.*, 2015, **289–290**, 379–392.
12 W.-C. Zheng and S.-Y. Wu, *Phys. Rev. B:Condens. Matter Mater. Phys.*, 1996, **54**, 1117–1122.
13 Q. Xiong, G. R. Bai and M. G. Zhao, *J. Appl. Phys.*, 1985, **57**, 3739–3739.
14 J. Krzystek, A. Ozarowski and J. Telser, *Coord. Chem. Rev.*, 2006, **250**, 2308–2324.
15 Ö. Üngör, T. M. Ozvat, J. V. Grundy and J. M. Zadrozny, in *Comprehensive Inorganic Chemistry III*, ed. J. Reedijk and K. R. Poeppelmeier, Elsevier, Oxford, 2023, pp. 745–770.
16 O. Kahn, *Molecular Magnetism*, John Wiley & Sons, New York, 1993.
17 S. Mugiraneza and A. M. Hallas, *Commun. Phys.*, 2022, **5**, 95.
18 V. Ivády, T. Simon, J. R. Maze, I. A. Abrikosov and A. Gali, *Phys. Rev. B:Condens. Matter Mater. Phys.*, 2014, **90**, 235205.
19 D. M. Toyli, C. F. de las Casas, D. J. Christle, V. V. Dobrovitski and D. D. Awschalom, *Proc. Natl. Acad. Sci. U. S. A.*, 2013, **110**, 8417–8421.
20 M. Y. Redko, R. Huang, J. L. Dye and J. E. Jackson, *Synthesis*, 2006, 759–761.
21 P. H. Smith, M. E. Barr, J. R. Brainard, D. K. Ford, H. Freiser, S. Muralidharan, S. D. Reilly, R. R. Ryan, L. A. Silks III and W. H. Yu, *J. Org. Chem.*, 1993, **58**, 7939–7941.
22 N. Alzakhem, C. Bischof and M. Seitz, *Inorg. Chem.*, 2012, **51**, 9343–9349.
23 G. M. Sheldrick, SADABS, University of Göttingen, Germany, 1996.
24 G. Sheldrick, *Acta Crystallogr., Sect. A:Found. Adv.*, 2015, **71**, 3–8.
25 G. Sheldrick, *Acta Crystallogr., Sect. C:Struct. Chem.*, 2015, **71**, 3–8.
26 G. Sheldrick, *Acta Crystallogr., Sect. A:Found. Crystallogr.*, 2008, **64**, 112–122.
27 O. V. Dolomanov, L. J. Bourhis, R. J. Gildea, J. A. K. Howard and H. Puschmann, *J. Appl. Crystallogr.*, 2009, **42**, 339–341.
28 C. F. Macrae, I. Sovago, S. J. Cottrell, P. T. A. Galek, P. McCabe, E. Pidcock, M. Platings, G. P. Shields, J. S. Stevens, M. Towler and P. A. Wood, *J. Appl. Crystallogr.*, 2020, **53**, 226–235.
29 G. A. Bain and J. F. Berry, *J. Chem. Ed.*, 2008, **85**, 532.
30 A. K. Hassan, L. A. Pardi, J. Krzystek, A. Sienkiewicz, P. Goy, M. Rohrer and L. C. Brunel, *J. Magn. Reson.*, 2000, **142**, 300–312.

31 S. Stoll and A. Schweiger, *J. Magn. Reson.*, 2006, **178**, 42–55.
32 G. A. Jeffrey, *An Introduction to Hydrogen Bonding*, Oxford University Press, 1997.
33 B. J. McNicholas, C. Nie, A. Jose, P. H. Oyala, M. K. Takase, L. M. Henling, A. T. Barth, A. Amaolo, R. G. Hadt, E. I. Solomon, J. R. Winkler, H. B. Gray and E. Despagnet-Ayoub, *Inorg. Chem.*, 2023, **62**, 2959–2981.
34 B. Figgis and M. Hitchman, *Ligand field theory and its applications*, Wiley-VCH, New York, 2000.
35 Y. Tanabe and S. Sugano, *J. Phys. Soc. Jpn.*, 1954, **9**, 766–779.
36 H. O. N. Reid, I. A. Kahwa, A. J. P. White and D. J. Williams, *Inorg. Chem.*, 1998, **37**, 3868–3873.
37 J. C. Hempel, R. A. Palmer and M. C. L. Yang, *J. Chem. Phys.*, 1976, **64**, 4314–4320.
38 J. Telser, *J. Biol. Inorg. Chem.*, 2022, **27**, 605–609.
39 C. Duboc, *Chem. Soc. Rev.*, 2016, **45**, 5834–5847.
40 T. A. Stich, S. Lahiri, G. Yeagle, M. Dicus, M. Brynda, A. Gunn, C. Aznar, V. J. DeRose and R. D. Britt, *Appl. Magn. Reson.*, 2007, **31**, 321–341.
41 T. J. Pearson, M. S. Fataftah and D. E. Freedman, *Chem. Commun.*, 2016, **52**, 11394–11397.
42 C. J. H. Jacobsen, E. Pedersen, J. Villadsen and H. Weihe, *Inorg. Chem.*, 1993, **32**, 1216–1221.
43 M. Azarkh, L. V. Penkova, S. V. Kats, O. A. Varzatskii, Y. Z. Voloshin and E. J. J. Groenen, *J. Phys. Chem. Lett.*, 2014, **5**, 886–889.
44 D. M. L. Goodgame, H. E. Mkami, G. M. Smith, J. P. Zhao and E. J. L. McInnes, *Dalton Trans.*, 2003, 34–35.
45 C. Duboc, M.-N. Collomb, J. Pécaut, A. Deronzier and F. Neese, *Chem. – Eur. J.*, 2008, **14**, 6498–6509.
46 C. Duboc, T. Phoeung, S. Zein, J. Pécaut, M.-N. Collomb and F. Neese, *Inorg. Chem.*, 2007, **46**, 4905–4916.
47 S. S. Eaton and G. R. Eaton, in *Distance Measurements in Biological Systems by EPR*, ed. L. J. Berliner, G. R. Eaton and S. S. Eaton, Springer, Boston, MA, 2002, vol. 19, pp. 29–154.
48 D. M. Duggan and D. N. Hendrickson, *Inorg. Chem.*, 1974, **13**, 2929–2940.
49 A. Solano-Peralta, J. P. Saucedo-Vázquez, R. Escudero, H. Höpfl, H. El-Mkami, G. M. Smith and M. E. Sosa-Torres, *Dalton Trans.*, 2009, 1668–1674.
50 B. Corzilius, V. K. Michaelis, S. A. Penzel, E. Ravera, A. A. Smith, C. Luchinat and R. G. Griffin, *J. Am. Chem. Soc.*, 2014, **136**, 11716–11727.
51 S. K. Misra, P. Giguère and G. R. Sharp, *J. Chem. Phys.*, 1977, **66**, 1758–1759.
52 M. V. Fedin, E. F. Zhilina, D. L. Chizhov, I. A. Apolonskaya, G. G. Aleksandrov, M. A. Kiskin, A. A. Sidorov, A. S. Bogomyakov, G. V. Romanenko, I. L. Eremenko, V. M. Novotortsev and V. N. Charushin, *Dalton Trans.*, 2013, **42**, 4513–4521.
53 Ö. Üngör, T. M. Ozvat, Z. Ni and J. M. Zadrozny, *J. Am. Chem. Soc.*, 2022, **144**, 9132–9137.
54 M. Rubín-Osanz, F. Lambert, F. Shao, E. Rivière, R. Guillot, N. Suaud, N. Guihéry, D. Zueco, A.-L. Barra, T. Mallah and F. Luis, *Chem. Sci.*, 2021, **12**, 5123–5133.
55 D. Gatteschi, R. Sessoli and J. Villain, *Molecular Nanomagnets*, Oxford University Press, New York, NY, 2006.
56 Y. Miyazaki, A. Bhattacharjee, M. Nakano, K. Saito, S. M. J. Aubin, H. J. Eppley, G. Christou, D. N. Hendrickson and M. Sorai, *Inorg. Chem.*, 2001, **40**, 6632–6636.
57 E. A. Suturina, J. Nehrkorn, J. M. Zadrozny, J. Liu, M. Atanasov, T. Weyhermüller, D. Maganas, S. Hill, A. Schnegg, E. Bill, J. R. Long and F. Neese, *Inorg. Chem.*, 2017, **56**, 3102–3118.
58 J. M. Zadrozny, S. M. Greer, S. Hill and D. E. Freedman, *Chem. Sci.*, 2016, **7**, 416–423.
59 (*a*) CCDC 2215553: Experimental Crystal Structure Determination, 2026, DOI: 10.5517/ccdc.csd.cc2dcggq; (*b*) CCDC 2215554: Experimental Crystal Structure Determination, 2026, DOI: 10.5517/ccdc.csd.cc2dcghr; (*c*) CCDC 2380186: Experimental Crystal Structure Determination, 2026, DOI: 10.5517/ccdc.csd.cc2kws6g.